Journal of Environmental Chemical Engineering 10 (2022) 107333

Contents lists available at ScienceDirect

Journal of Environmental Chemical Engineering

journal homepage: www.elsevier.com/locate/jece

Highly efficient and selective removal of Sr^{2+} from aqueous solutions using ammoniated zirconium phosphate

Zeqiu Li [a], Eleazer L. Vivas [a], Yong Jae Suh [b,c,*], Kuk Cho [a,**]

[a] Department of Environmental Engineering, Pusan National University, 2 Busandaehak-ro 63beon-gil, Geumjeong-gu, Busan 46241, Republic of Korea
[b] Mineral Resources Research Division, Korea Institute of Geoscience and Mineral Resources, 124 Gwahak-ro, Yuseong-gu, Daejeon 34132, Republic of Korea
[c] Department of Resources Recycling, Korea University of Science and Technology, 217 Gajeong-ro, Yuseong-gu, Daejeon 34113, Republic of Korea

ARTICLE INFO

Editor: Apostolos Giannis

Keywords:
Adsorption
Ion exchange
Radionuclide
Strontium-90
Ammonium intercalation

ABSTRACT

Radioactive wastewater contains high concentrations of ^{90}Sr (strontium-90), which poses a serious threat to human health and ecosystems. Layered ammoniated zirconium phosphate (A-ZrP) was synthesized herein using a one-pot hydrothermal method for the adsorptive removal of Sr^{2+}. ZrP was ammoniated between its structured layers to increase interlayer spacing and facilitate the access of Sr^{2+} ions to adsorption sites and realize adequate ion exchange. A-ZrP achieved a faster equilibration time (120–240 min) compared with that of other ZrPs (250–500 min). A-ZrP exhibited excellent Sr^{2+} uptake selectivity (K_d = 5.3 × 10^5 mL g^{-1}) and maximum adsorption capacity (q_m = 341 mg g^{-1}) at a pH of 7. Moreover, A-ZrP displayed high selectivity in various contaminated solutions, with a high K_d value of 681 mL g^{-1}, even in artificial seawater. The adsorption mechanism was found to involve ion exchange between NH_4^+ and Sr^{2+}, primarily because of electrostatic interactions and chemical hardness. These results highlight the potential of A-ZrP as an efficient adsorbent for the selective removal of Sr^{2+} ions from wastewater.

1. Introduction

Nuclear energy has attracted significant attention owing to the ongoing global energy crisis. However, the use of nuclear energy generates various radionuclide pollutants [1], which are detrimental to the environment and human health if accidentally released or improperly managed. For example, a large amount of ^{90}Sr (strontium-90)-containing wastewater was produced after the Fukushima nuclear accident in 2011 [2]. ^{90}Sr is known to be an extremely toxic radionuclide with a half-life of over 28.78 years [3]. Possessing calcium-like properties, ^{90}Sr can be easily transported by water into the human body and accumulate in bones, causing rickets, cancers, and other serious diseases; thus, it should be completely removed from wastewater [4,5].

Various water purification strategies based on physical, chemical, and biological principles have been adopted for strontium removal from contaminated water [6]. Owing to its high removal efficiency, low cost, and availability of a wide variety of adsorbents, adsorption has become a promising technique for capturing water pollutants in trace levels. Among the various adsorbents, inorganic materials, such as zeolites [7,8], hydrated oxides [9,10], metal sulfides [11,12], and titanate-based materials [13,14], have been used for strontium removal.

Crystalline zirconium phosphates (ZrPs) have attracted considerable interest as potential adsorbents. The space between the layers of ZrPs, which is an important attribute that influences the adsorption capacity and selectivity of layered inorganic frameworks, can be altered to facilitate the removal of a target metal ion from wastewater. The protons in the phosphate groups of ZrPs can be readily replaced by various cations with significantly larger ionic radii than that of protons, thereby enlarging the interlayer distance. This approach has been exploited to fabricate layered sodium γ-zirconium phosphate ($NaHZr(PO_4)_2{\cdot}xH_2O$)

Abbreviations: ZrP, Zirconium phosphate; A-ZrP, ammoniated zirconium phosphate; XRD, X-ray diffraction; FTIR, Fourier transform infrared spectroscopy; TGA, thermogravimetric analysis; DTG, derivative thermogravimetry; EDS, energy-dispersive X-ray spectroscopy; TW, tap water; NMW, natural mineral water; ASW, artificial seawater; DIW, deionized water; AAS, atomic absorption spectrometry; FE-SEM, field emission scanning electron microscopy; PFO, pseudo first order; PSO, and pseudo second order.

* Corresponding author at: Mineral Resources Research Division, Korea Institute of Geoscience and Mineral Resources, 124 Gwahak-ro, Yuseong-gu, Daejeon 34132, Republic of Korea.
** Corresponding author.
E-mail addresses: aumsuh@kigam.re.kr (Y.J. Suh), kukcho@pusan.ac.kr (K. Cho).

https://doi.org/10.1016/j.jece.2022.107333
Received 1 October 2021; Received in revised form 17 January 2022; Accepted 3 February 2022
Available online 4 February 2022

[15] and disodium zirconium phosphate ($Zr(NaPO_4)_2{\cdot}H_2O$) [16], which exhibited effective adsorptive removal of Cs^+ and heavy metal ions, such as Tl^+, Pb^{2+}, Cu^{2+}, and Cd^{2+}, from water, respectively. In particular, flower-like Na^+-intercalated α-ZrP [17] and 4-amino-benzo-18 crown 6-intercalated α-ZrP [18] demonstrated enhanced adsorption capacities for Sr^{2+}, with the latter exhibiting an adsorption capacity of 320.1 mg g^{-1}; however, two additional steps were required for intercalation, with each step lasting six days.

Ammonium ions were intercalated in ZrP in the present study for the first time and exchanged with Sr^{2+}. It should be noted that although NH_4^+-intercalated ZrP has been synthesized for producing γ-ZrP, its ion-exchange behavior has not been investigated [19]. The ionic radius of the ammonium ion (1.40–1.67 Å [20]) is greater than those of Na^+ (0.99–1.39 Å) and Sr^{2+} (1.18–1.44 Å) [21], which could result in a wider interlayer spacing of NH_4^+-intercalated ZrP. During ammonium intercalation, remnant ammonia molecules can also reside in layered structures as guest molecules [22]. Therefore, ZrPs can contain a large amount of ammonia, which results in an increased interlayer distance [23]. The wider interlayer spacing of ZrPs can favor Sr^{2+} ion exchange owing to the presence of both ammonium ions and ammonia. The adsorptive sites of ammoniated ZrP (A-ZrP) can facilitate stronger electrostatic interactions with divalent Sr^{2+} ions compared with those of NH_4^+. Furthermore, Sr^{2+}, which is a harder acid than NH_4^+, binds to O, which is a hard base element, of A-ZrP according to the concept of hard-soft acid-base theory [24,25]. Therefore, the straightforward exchange of ammonium ions that occupy the adsorptive sites prior to Sr^{2+} adsorption with harder Sr^{2+} ions was hypothesized to occur in this study.

Layered crystalline A-ZrP was prepared via a facile and environmentally benign 24-h one-pot hydrothermal method for the removal of strontium from water. The influences of pH, adsorbent dose, initial Sr^{2+} concentration, contact time, and coexisting ions on the strontium removal capability of A-ZrP were investigated. A-ZrP exhibited an excellent Sr^{2+} adsorption selectivity of 5.3×10^5 mL g^{-1} at a pH of 7. The Sips isotherm model adequately fits the Sr^{2+} adsorption data, resulting in a maximum capacity of 341 mg g^{-1}. Therefore, A-ZrP was found to be a promising material for removing radioactive Sr from water.

2. Experimental

All experiments were performed in triplicate unless otherwise indicated.

2.1. Reagents

Zirconyl(VI) chloride octahydrate ($ZrOCl{\cdot}8H_2O$, 98%) and ammonium phosphate trihydrate ($(NH_4)_3PO_4{\cdot}3H_2O$, 95%) were purchased from Acros Organics (India) and Kanto Chemical Co., Inc. (Japan), respectively. HCl (35–37 wt%), NaOH (98%), NH_4F (95%), NaCl (99.5%), KCl (99%), $MgCl_2{\cdot}6H_2O$ (98%), $CaCl_2{\cdot}6H_2O$ (98%), and $SrCl_2{\cdot}6H_2O$ (98.5%) were supplied by Daejung Chemical and Metals Co., Ltd (Republic of Korea). All chemicals and reagents were used as received without further purification.

2.2. Preparation of layered A-ZrP

Using Zr:P:F molar ratios ($ZrOCl_2{\cdot}8H_2O$:$(NH_4)_3PO_4{\cdot}3H_2O$:NH_4F) of 1:P:0.3, where P = 2–8, $ZrOCl_2{\cdot}8H_2O$ (1.063 g), $(NH_4)_3PO_4{\cdot}3H_2O$, and NH_4F (0.037 g) powders were ground and mixed using an agate mortar and pestle for 30 min. The resulting paste was transferred into a 100-mL Teflon-lined autoclave reactor and heated at a temperature (T) of 120 °C for 24 h, and subsequently allowed to cool to room temperature prior to collecting the product (Fig. S1). The synthesized solid particles were washed with deionized water (DIW) three times through centrifugation at 10,000 rpm (11,057 RCF) for 10 min, oven-dried in air at 60 °C for 48 h, ground with an agate mortar and pestle, and stored in a dry glass vial. NH_4F was employed in the synthesis of A-ZrP because it facilitates the formation of highly crystalline α-ZrP particles [26]. The scheme of A-ZrP synthesis is provided in the Supporting Information (Fig. S1).

The mechanism of A-ZrP formation is described henceforth. Heating promotes the replacement of protons with NH_4^+ during crystallization [23]. Zirconium salts react with ammonium orthophosphate, during which a portion of the ammonium phosphate decomposes and releases NH_3, which infiltrates the ZrP layers and bonds with phosphate groups to form NH_4^+ ions. This reaction is summarized as follows (Eq. (1)):

$$Zr(HPO_4)_2{\bullet}nH_2O + NH_3 \leftrightarrow Zr(NH_4PO_4)(HPO_4){\bullet}nH_2O \quad (1)$$

2.3. Material characterization

The structural characteristics of A-ZrP at different stages were probed by X-ray diffraction (XRD) using an X′pert^3 diffractometer (Malvern Panalytical Ltd., United Kingdom; Cu Kα beam, $\lambda = 0.154$ nm, 40 kV, 30 mA). The surface functional groups and chemical bonds of the samples were characterized by Fourier transform infrared spectroscopy (FTIR; Shimadzu, Japan) within 500–4000 cm^{-1}. The thermal stability of the adsorbent was determined by thermogravimetric analysis (TGA; SDTQ600 TA Instruments, United States) in a nitrogen atmosphere from 20 °C to 800 °C at a nitrogen flow rate of 20 mL min^{-1} and a heating rate of 10.0 °C min^{-1}. The surface morphologies of the prepared samples were characterized by field-emission scanning electron microscopy (FE-SEM; SUPRA25, Germany). The elemental mapping of the samples was investigated by energy-dispersive X-ray spectroscopy (EDS) using an X-ray spectrometer with a MIRA 3 LMH In-Beam EDS detector (Zeiss, Germany). The pH of the aqueous solutions was probed using a portable pH meter (Orion Star A Series X21407, Thermo Scientific, Indonesia).

2.4. Batch adsorption experiments

To avoid radiation exposure, non-radioactive Sr^{2+} ions were used as a substitute for ^{90}Sr. The former and latter are expected to possess similar chemical properties. $SrCl_2{\cdot}6H_2O$ was dissolved in DIW to prepare aqueous solutions of Sr^{2+} at different concentrations. Using a solid-to-liquid ratio (S/L) of 0.5 g L^{-1}, 10 mg of the A-ZrP powder was immersed in 20 mL of the aqueous Sr^{2+} solution and shaken at 150 rpm for 24 h using an orbital shaker (Digital Orbital Shaker, SHO-2D, South Korea). All adsorption experiments were conducted at room temperature ($T = 25$ °C), unless otherwise specified.

The adsorption capacity (q_e in mg g^{-1}) was calculated using Eq. (2), where C_o (mg L^{-1}) is the initial concentration of Sr^{2+}, C_e (mg L^{-1}) is the equilibrium concentration, m (g) is the mass of the A-ZrP powder, and V (L) is the volume of the aqueous Sr^{2+} solution.

$$q_e = \frac{C_o - C_e}{m} \times V \quad (2)$$

The Sr^{2+} uptake kinetics at $C_o = 100$ mg L^{-1} were evaluated using Eq. (3), where q_t is the q_e of A-ZrP and C_t is the Sr^{2+} concentration after a certain contact time (t = 1–1440 min). Pseudo-first-order (PFO) and pseudo-second-order (PSO) models were employed to analyze the results of the adsorption kinetics experiment by nonlinear fitting [27] (Eqs. (4) and (5), respectively). The goodness of fit of the nonlinear regressions of the experimental adsorption kinetics data was determined using the correlation coefficient (r^2) value.

$$q_t = \frac{C_o - C_t}{m} \times V \quad (3)$$

$$q_t = q_e\left(1 - e^{-k_1 t}\right) \quad (4)$$

$$q_t = \frac{k_2 q_e^2 t}{1 + k_2 q_e t} \quad (5)$$

Here, k_1 (min^{-1}) and k_2 (g mg^{-1} min^{-1}) are the PFO and PSO rate constants, respectively.

Equilibrium batch adsorption experiments were conducted at different initial concentrations of Sr^{2+} (C_o = 10–1000 mg L^{-1}). The Langmuir, Freundlich, and Sips isotherm models, expressed by Eqs. (6), (7), and (8), respectively, were used for nonlinear fitting of the Sr^{2+} adsorption data. Values of the r^2 were used to determine the goodness of fit of the nonlinear regression models.

$$q_e = \frac{q_m K_L C_e}{1 + K_L C_e} \quad (6)$$

$$q_e = K_F C_e^{\frac{1}{n_F}} \quad (7)$$

$$q_e = \frac{q_m K_S C_e^{\frac{1}{n_S}}}{1 + K_S C_e^{\frac{1}{n_S}}} \quad (8)$$

Here, q_m (mg g^{-1}) represents the maximum adsorption capacities, respectively; K_L (L mg^{-1}), K_F (mg g^{-1}(L $mg^{-1})^{1/n}$), and K_S (mg g^{-1}) are the Langmuir, Freundlich, and Sips constants, respectively; and n_F and n_S are dimensionless factors pertaining to the Freundlich and Sips adsorption, respectively.

The influence of C_o on the removal efficiency (R) was calculated using Eq. (9).

$$R \quad (\%) = \frac{C_o - C_e}{C_o} \times 100 \quad (9)$$

The effect of pH on the adsorption of Sr^{2+} was examined using 100 mg L^{-1} aqueous solutions of Sr^{2+} with an initial pH of 1–11. An aqueous solution of 0.5 M NaOH or 0.5 M HCl was employed to adjust the pH.

The distribution coefficient (K_d, mL g^{-1}) of the adsorption selectivity for Sr^{2+} in different environments was estimated using Eq. (10). Interference tests were conducted with 10 mg L^{-1} Sr^{2+} solutions by adding different concentrations of foreign ions, including 1–100 mmol L^{-1} aqueous Na^+, K^+, Mg^{2+}, and Ca^{2+} solutions, tap water (TW), natural mineral water (NMW; Jeju Samdasoo, Republic of Korea), and artificial seawater (ASW; Coralife, USA). TW, NMW, and ASW have varying concentrations of the aforementioned background cations (Table S1). The influence of coexisting ions was analyzed by measuring the residual concentration of Sr^{2+} after equilibrium was achieved.

$$K_d = \frac{C_0 - C_e}{C_e} \times \frac{V}{m} \quad (10)$$

2.5. Chemical analysis

The liquid samples of the adsorption experiments were filtered and transferred into 50-mL conical sample tubes using 0.22-μm cellulose acetate syringe filters. Adequate amounts of the liquid samples were diluted in volumetric flasks containing 0.2% w/v K^+ (from KCl) and 2.5 wt% HNO_3. Strontium concentrations were determined by a flame atomic absorption spectroscopy (AAS; AAnalyst 200, USA). About 5 mL of a collected liquid sample was used for pH measurement, and the remaining volume is stored in a cooling chamber maintained at 2 °C.

3. Results

3.1. Effect of phosphate content on Sr^{2+} uptake capacity

The influence of the molar proportion of $(NH_4)_3PO_4$•$3H_2O$ during A-ZrP synthesis on Sr^{2+} adsorption capacity was investigated. Fig. 1(a) indicates that the q_e value at C_o = 500 mg L^{-1} increases with an increase in the amount of $(NH_4)_3PO_4$•$3H_2O$ up to 6.0 mol and subsequently declines. The addition of more $(NH_4)_3PO_4$•$3H_2O$ (> 6.0 mol) reduces the crystallinity, which is presumably responsible for this decline, and possibly results in the partial collapse of the layered structure (Fig. S2). Therefore, an optimal molar ratio of 1:6:0.3 for $ZrOCl_2$•$8H_2O$:$(NH_4)_3PO_4$•$3H_2O$:NH_4F was used in the synthesis of crystalline A-ZrP adsorbent powders for subsequent experiments.

3.2. Characteristics of the A-ZrP adsorbent powder

The FE-SEM images in Fig. 2(a) and (b) show whisker-like A-ZrP particles that are 200–400 nm in width and several micrometers in length. The elemental maps and energy spectrum (Fig. 2(c)) reveal homogeneous distributions of Zr, N, P, and O, and a Zr/P ratio of 0.34. Fig. 2(d) indicates that the post-adsorption A-ZrP particles contain a large amount of homogeneously distributed Sr with a Sr/Zr atomic percent ratio of 1.9, whereas the atomic percent composition of nitrogen reduces to 25% compared to that of pristine A-ZrP. Although the EDS energy spectrum is generally considered a semiquantitative analysis, the overall behavior of the adsorption can be accounted for.

The FTIR spectrum of the as-prepared A-ZrP (Fig. 3(a)) shows characteristic peaks at 935, 990, and 1062 cm^{-1} due to P–O stretching vibrations [28]; spectral peaks at 555 cm^{-1} and 629 cm^{-1} corresponding to the Zr–O bonds [29]; and a spectral peak at 1435 cm^{-1} representing N–H bonds [30]. The spectral peak intensity corresponding to the N–H bonds significantly decreases after Sr adsorption, indicating a decrease in the content of corresponding materials, that is, either NH_3 or NH_4^+. However, an additional peak at 653.5 cm^{-1} corresponding to Sr–O bonds does not appear.

The TGA curve (Fig. 3(b)) reveals three- and one-step weight losses with respect to temperature for the pristine and Sr^{2+}-loaded A-ZrP

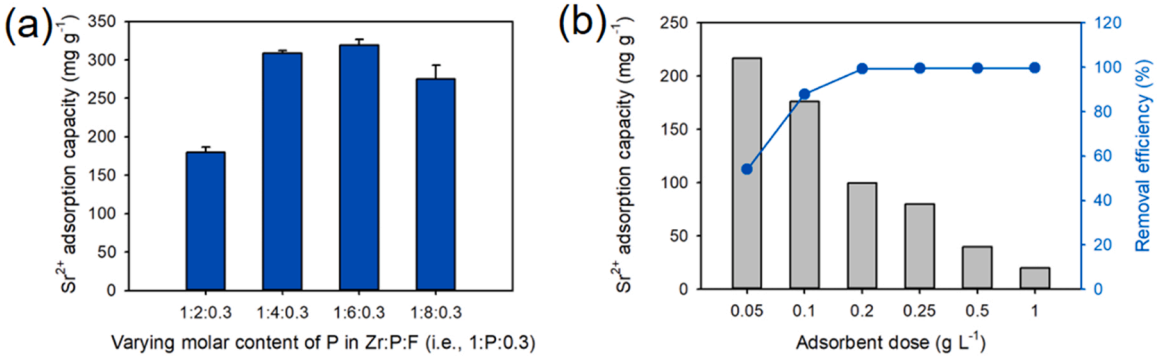

Fig. 1. Effects of (a) $(NH_4)_3PO_4$•3 H_2O dose in A-ZrP synthesis (C_o ≅ 500 mg L^{-1}, pH = 5.5, S/L = 1.0 g L^{-1}, t = 1440 min) and (b) adsorbent dose (C_o ≅ 20 mg L^{-1}, pH = 7, t = 1440 min) on the Sr^{2+} adsorption capacity. General adsorption conditions: T = 25 °C, shaking rate = 150 rpm.

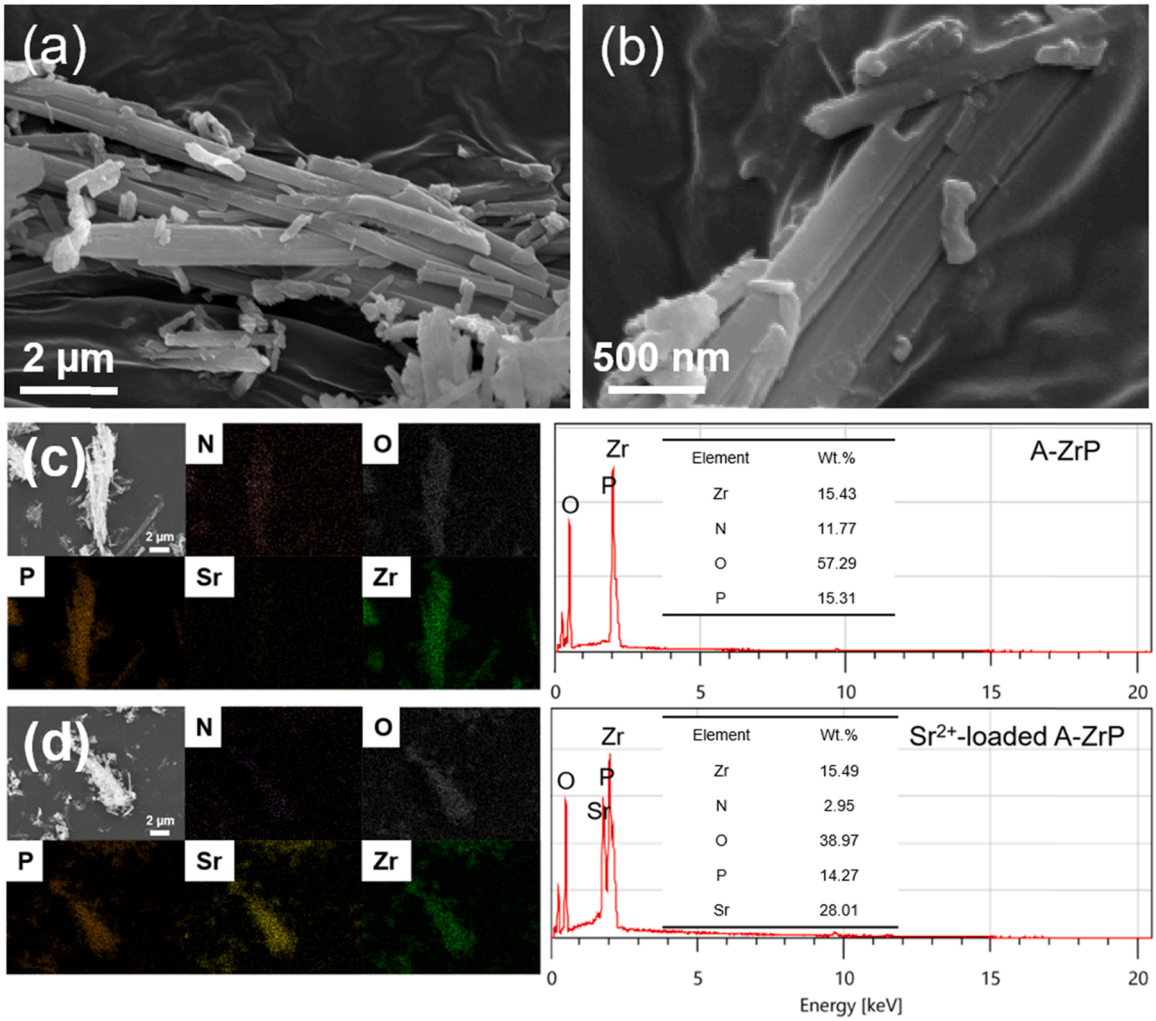

Fig. 2. FE-SEM images and EDS analysis: FE-SEM images of A-ZrP at (a) low and (b) high magnifications; SEM–EDS mapping and energy spectra (inset: elemental wt %) of (c) pristine A-ZrP and (d) A-ZrP after Sr^{2+} adsorption.

whiskers, respectively. In the pristine A-ZrP sample, the first stage weight loss (16%) from 25° to 100°C is due to the evaporation of water and NH_3 molecules. The second stage weight loss (22%) can also be attributed to NH_3 evaporation because of the presence of two types of ammonia absorption sites on ZrP [23]. The third weight loss (10%) at $T > 540$ °C can be attributed to the condensation of phosphate groups [31]. However, a continuous single-step weight loss (27%) occurs in the Sr^{2+}-loaded A-ZrP sample, resulting from simultaneous dehydration, decomposition of residual NH_3 and NH_4^+, and condensation of phosphate groups [31]. The total weight losses incurred upon heating the pristine and Sr^{2+}-loaded A-ZrPs at 800 °C are 48% and 27%, respectively. The lower weight-loss percentage of the latter is due to the replacement of more volatile NH_3 molecules and NH_4^+ ions with Sr^{2+} ions during adsorption. The derivative thermogravimetry (DTG) profile (Fig. 3(c)) shows three peaks ($T = 97$, 267, and 585 °C) corresponding to the aforementioned weight losses.

The XRD patterns depicted in Fig. 3(d) confirm the crystallinity of the as-prepared and Sr^{2+}-saturated A-ZrPs. The possible adsorption of Sr^{2+} ions within the A-ZrP interlayers was qualitatively and partially confirmed by evaluating the lattice spacing (d) values of the adsorbent before and after adsorption using Bragg's law (Eq. (11)).

$$d = \frac{\lambda}{2\sin\left(\frac{2\theta}{2}\right)} \tag{11}$$

Here, λ is the X-ray wavelength during XRD analysis (0.154 nm), and 2θ (°) is the position of the Bragg diffraction peak in the XRD pattern.

The position of 2θ corresponding to the most intense Bragg peak slightly shifts to the right from 10.6° to 11.1° in Sr^{2+}-loaded A-ZrP, indicating the contraction of d from 8.34 Å to 7.96 Å. The decreased interlayer space can be attributed to the exchange of larger NH_4^+ ions with smaller Sr^{2+} ions.

3.3. Sr^{2+} adsorption behavior of A-ZrP

The effect of adsorbent dose on Sr^{2+} uptake was first examined to determine the appropriate dose for a systematic investigation of adsorption. Fig. 1(b) shows that the removal efficiency (R) increases with increasing adsorbent doses from 0.05 to 0.20 g L^{-1} because the number of adsorption sites is proportional to the quantity of adsorbent used. The removal efficiency saturates at 99.4% at a dose $\geq$ 0.20 g L^{-1}. By contrast, the adsorption capacity decreases as the adsorbent dose increases. This indicates that more adsorption sites remain unoccupied at a constant amount of the adsorbate as the dose increases.

The pH has a significant effect on the surface charge of the adsorbent and particle stability. In addition, the ions used for adjusting the pH compete for the adsorption sites, thereby affecting the Sr^{2+} uptake capability. The point of zero charge (pH_{pzc}) of A-ZrP is most likely similar to that of the flower-like Na^+-intercalated ZrP ($pH_{pzc} \cong 2.75$) [17], as both of them are α-ZrPs. This is corroborated by A-ZrP

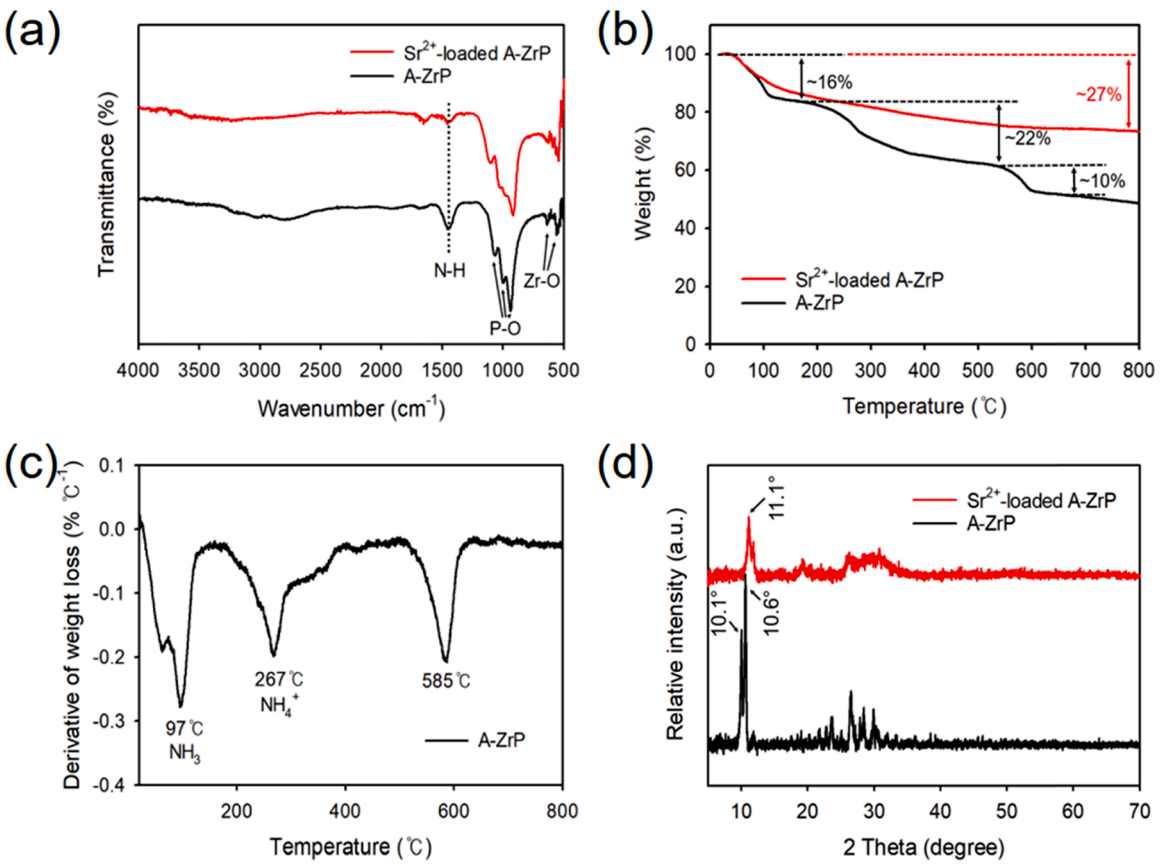

Fig. 3. Characteristics of the as-prepared and Sr-loaded A-ZrPs: (a) FTIR spectra, (b) TGA curves, (c) DTG plot, and (d) XRD patterns.

exhibiting high values of R (> 96.0%) in the pH range of 3–11 (Fig. 4 (a)). The greater number of negatively charged surfaces of the ZrP material at pH > pH_{pzc} leads to a higher cation adsorption rate. The relatively lower q_e value observed at pH ≅ 1.0 can be attributed to the slight electrostatic repulsion between A-ZrP particles and Sr^{2+} ions due to the (1) partial positive surface charge of A-ZrP and (2) presence of competitive H^+ ions at this extremely acidic condition. A pH of 7.0 is optimal for Sr^{2+} adsorption, owing to its high values of R (> 99.6%) and K_d (> 5.3×10^5 mL g^{-1}). The value of K_d is significantly low at a pH of 1.0 (2.5×10^3 mL g^{-1}), with H^+ strongly competing with Sr^{2+} for NH_4^+-ion exchange. Additionally, the destruction of the layered structure at a pH of 1.0 accounts for the reduction in ion exchange (Fig. S3). However, the K_d values of A-ZrP under acidic conditions are higher than those of other adsorbents, such as alginate microspheres and poly (amidoxime)-modified reduced graphene oxide (PAO-G-RGO), which have K_d < 1.0 at a pH of 1 and 2, respectively [33,34]. Because Sr is present in the form of Sr^{2+} ions at a pH below 12, according to the speciation diagram shown in Fig. S4, the possibility of Sr removal by precipitation can be eliminated. These results demonstrate that the A-ZrP powders can effectively remove Sr^{2+} ions from aqueous solutions over a wide range of pH (3–11). A pH of 7.0 was selected as the optimal value for the subsequent adsorption experiments.

Adsorption isotherms are typically employed to describe the surface properties and affinity of adsorbents and evaluate the maximum adsorption capacity (q_m) of adsorbents.

Fig. 4(b) indicates that A-ZrP almost saturates at $C_e \geq 650$ mg L^{-1} (considering the error bars); moreover, the Sips model provides an excellent fit to the Sr^{2+} adsorption isotherm owing to its highest r^2 value of 0.9646 among the three models (Table 1). Because the Langmuir model does not adequately describe the adsorption of Sr^{2+} by A-ZrP, the surface is presumably not homogeneous for adsorption, and multilayer adsorption occurs. This is also supported by the computed n_S value of 2.3563, which is far from unity. The calculated maximum Sips adsorption capacity of A-ZrP for Sr^{2+} was 341 mg g^{-1}; this value is considered for the comparison described in the discussion section.

Adsorption experiments with varying contact times were subsequently performed to elucidate the kinetics of Sr^{2+} adsorption on A-ZrP. Fig. 4(c) indicates that the adsorption rate is high and reaches R > 92.4% within 30 min only; equilibrium is achieved in 120–240 min (R > 99.6%). The adsorption kinetics are confirmed to follow the PSO model because of its higher r^2 (0.9774) than that (0.9136) of the PFO model (Table S2). A-ZrP has faster Sr^{2+} uptake rate than previously investigated ZrPs as discussed in Section 4.1.

Nuclear wastewater is an extremely complicated system in which Sr^{2+} adsorption can be hindered by competing cations, such as Na^+, K^+, Mg^{2+}, and Ca^{2+}. Fig. 4(d) shows that A-ZrP can remove 99.6% ($K_d = 4.7 \times 10^5$ mL g^{-1}) of Sr^{2+} ions from a single-component aqueous solution without competing ions (i.e., Sr^{2+}-spiked DIW). However, the values of R and K_d decrease as the concentration of the competing divalent cations increases. The presence of Na^+ and K^+ ions does not significantly affect the values of R and K_d. R slightly decreases to 99.1% ($K_d = 2.1 \times 10^5$ mL g^{-1}) and 98.1% ($K_d = 1 \times 10^5$ mL g^{-1}) in 100 mmol L^{-1} aqueous Na^+ and K^+ solutions, respectively. However, the values of R corresponding to the Mg^{2+} and Ca^{2+} solutions at concentrations of 1 and 100 mmol L^{-1} decrease from 99.4% ($K_d = 4.2 \times 10^5$ mL g^{-1}) to 45.8% ($K_d = 1.7 \times 10^3$ mL g^{-1}), and from 95.5% ($K_d = 4.4 \times 10^4$ mL g^{-1}) to 2.5% (K_d = 51.4 mL g^{-1}), respectively. Ca^{2+} ions at concentrations ≥ 10 mmol L^{-1} cause a remarkable decline in Sr^{2+} adsorption compared to Mg^{2+}. These results indicate that high concentrations of Ca^{2+} and Mg^{2+} strongly compete with Sr^{2+} for the adsorption sites of A-ZrP. The inhibitory effect of coexisting ions on Sr^{2+} removal by A-ZrP follows the $Ca^{2+} > Mg^{2+} >> K^+ > Na^+$ trend.

Different types of water in natural environments contain different levels of coexisting ions. Therefore, it is necessary to explore the effect of

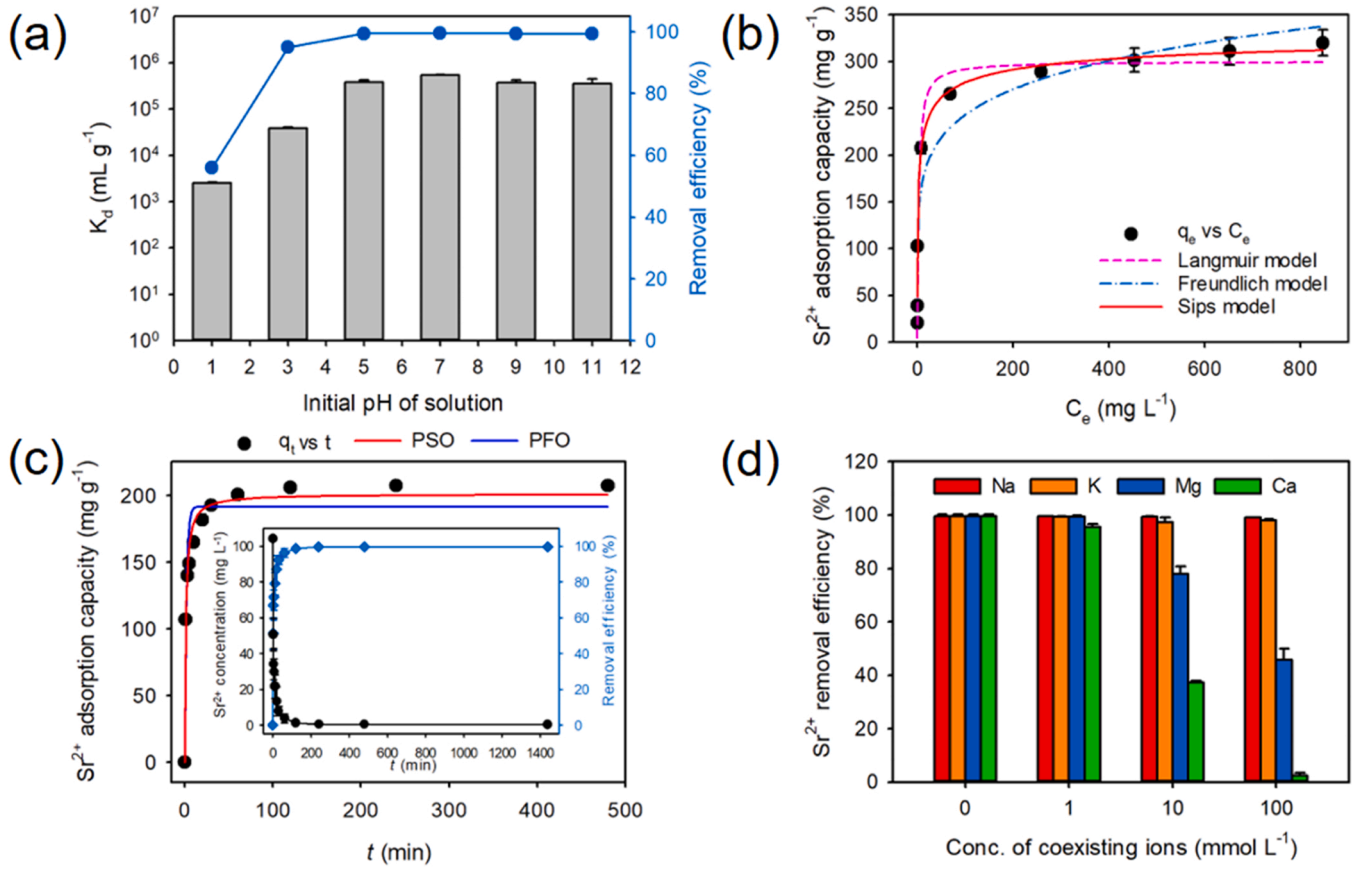

Fig. 4. Sr^{2+} adsorption performance of A-ZrP: (a) effect of pH on the distribution coefficient ($C_o \cong$ 100 mg L^{-1}, pH = 1–11, t = 240 min), (b) influence of initial concentration on the adsorption capacity (C_o = 10–1000 mg L^{-1}, pH = 7, t = 1440 min), (c) effect of contact time on the adsorption capacity (C_o = 100 mg L^{-1}, pH = 7.0, t = 1–1440 min), and (d) influence of coexisting ions (Na^+, K^+, Mg^{2+}, and Ca^{2+}) on the removal efficiency ($C_o \cong$ 10 mg L^{-1}, pH = 7.0, t = 240 min). General adsorption conditions: T = 25 °C, S/L = 0.5 g L^{-1}, shaking rate = 150 rpm.

Table 1
Adsorption isotherm constants for Sr^{2+} on A-ZrP powders.

Model	Parameter	Value
Langmuir	q_m (mg g^{-1})	300
	K_L (L mg^{-1})	0.358
	r^2	0.887
Freundlich	K_F (mg g^{-1}(L mg^{-1})$^{1/n}$)	120
	n_F	6.52
	r^2	0.915
Sips	q_m (mg g^{-1})	341
	K_S (L mg^{-1})	0.627
	n_S	2.36
	r^2	0.965

actual water environments on Sr^{2+} removal by A-ZrP. Fig. S5 suggests that the R values of A-ZrP in DIW, TW, NMW, and ASW are 99.6% (K_d = 4.7 × 10^5 mL g^{-1}), 99.9% (K_d = 8.3 × 10^6 mL g^{-1}), 99.8% (K_d = 1.7 × 10^6 mL g^{-1}), and 25.4% (K_d = 681 mL g^{-1}), respectively. A-ZrP performed better than several other Sr^{2+} adsorbents, including titanate nanotubes [14] and alginate/Fe_3O_4 composites [35] (Table S3). Overall, A-ZrP retains excellent Sr^{2+} adsorption performance even in the presence of large amounts of coexisting ions, specifically Na^+ and K^+.

4. Discussion

4.1. Effect of increased interlayer spacing

NH_4^+ and possibly leftover NH_3 expand the interlayer spacing of A-ZrP (8.34 Å, Fig. 3(d)) more than that of the flower-like Na^+-intercalated α-ZrP (7.6 Å) [17]; because the predominant species of nitrogen at pH < 9.2 is presumed to be NH_4^+, the amount of NH_3 cannot be dominant. The larger interlayer spacing of A-ZrP results in faster Sr^{2+} adsorption kinetics. Adsorption equilibrium is achieved in 120–240 min with A-ZrP (Fig. 4(c)), whereas it is realized in 250–500 min with the flower-like Na^+-intercalated α-ZrP [17]. The considerably larger interlayer spacing of 29.6 Å in 4-amino-benzo-18 crown 6-intercalated α-ZrP did not contribute to the kinetics (equilibration time ≅ 300 min), probably because of an adsorption mechanism involving complexation, which might be different from ours [18].

The expanded interlayer space of A-ZrP also enhances the maximum adsorption capacity (341 mg g^{-1}), which is higher than that of flower-like Na^+-intercalated α-ZrP (293.4 mg g^{-1}) [17]; the 4-amino-benzo-18 crown 6-intercalated α-ZrP exhibited a q_m of 320.1 mg g^{-1} [18]. Table S4 suggest that the maximum adsorption capacity of A-ZrP (q_m = 341 mg g^{-1}) is significantly higher than those of several previously reported adsorbents, such as α-ZrP (166.0 mg g^{-1}) [32], α-ZrP-SO_3H (183.2 mg g^{-1}) [36], Na-titanate nanobelts (238.3 mg g^{-1}) [14], NaFeTiO (233.5 mg g^{-1}) [13], spent coffee grounds biochars (41.2 mg g^{-1}) [37], and layered thiostannate (141.2 mg g^{-1}) [38]. However, it is lower than those of alginate/Fe_3O_4 (416.7 mg g^{-1}) [35] and the graphene oxide-hydroxyapatite (GO-HAp) composite (702.2 mg g^{-1}) [39]. Alginate/Fe_3O_4 exhibited an equilibration time of 6 h, which is considerably longer than that of A-ZrP. The GO-HAp composite required seven days of incubation during synthesis and exhibited a K_d of the order of 10^3 mL g^{-1}, which corresponds to a selectivity that is approximately three orders of magnitude lower than that of A-ZrP. A comparison of the q_m and K_d values of various adsorbents is challenging because of variations in the experimental conditions

of the corresponding studies. Nevertheless, A-ZrP exhibits a better adsorption performance than several Sr^{2+} adsorbents.

4.2. Adsorption mechanism

FTIR, EDS, and XRD analyses were considered to explore the mechanism of Sr^{2+} adsorption on A-ZrP. The FTIR spectra in Fig. 3(a) show a significantly weaker N–H peak (1435 cm^{-1}) after Sr^{2+} adsorption, and the EDS mapping in Fig. 2(d) reveals the considerable decrease in N content and the uniform distribution of a large amount of Sr^{2+} on the adsorbent surface. These two results confirm the replacement of the interlayer NH_4^+ ions with Sr^{2+}.

The intercalation of NH_4^+ and the successive exchange with Sr^{2+} were further elucidated by analyzing XRD patterns of the as-prepared A-ZrP, A-ZrP washed further for 1 and 4 h, and Sr^{2+}-adsorbed A-ZrP (Fig. 5). The primary XRD peaks of the as-prepared A-ZrP did not match those of standard $Zr(NH_4PO_4)(HPO_4)\cdot 0.3H_2O$ (ICDD #00–032–1488). The low-angle peaks (at 10.1° (8.75 Å) and 10.6° (8.34 Å)) depicted in Fig. 5(a) shift to the left, in comparison with those in the standard spectrum (11.1° (7.96 Å) and 11.8° (7.49 Å)) shown at the bottom in Fig. 5; this is due to the presence of excess NH_4^+. Fig. 5(b) shows new peaks at 11.1° and 11.8° for the sample washed further with DIW for 1 h. When A-ZrP is placed in DIW, free or weakly bonded NH_4^+ ions between the adsorbent layers are continuously released into the bulk water outside A-ZrP, which reduces the interlayer spacing of certain adsorbent particles. The peaks representing the sample washed further for 4 h at 10.1° and 10.6°, which correspond to the large interlayer spacing, completely disappear (Fig. 5(c)), and the primary XRD peaks coincide with those of the standard spectrum of $Zr(NH_4PO_4)(HPO_4)\cdot 0.3H_2O$. The primary peaks corresponding to the as-prepared A-ZrP particles placed in a Sr^{2+}-rich solution appear at 11.1° (7.96 Å) (Fig. 5(d)). This can be attributed to the presence of adsorbed Sr^{2+} ions that replace NH_4^+, which results in a smaller interlayer spacing than that of A-ZrP because of the smaller ionic radius of Sr^{2+} (1.18–1.44 Å [21]) than that of NH_4^+ (1.40–1.67 Å [20]). In the course of the additional water washing, ammonium ions tend to diffuse out of the interlayer spacing in the absence of competing species such as Sr^{2+} when the concentration gradient exists. The resulting empty sites should be protonated again to neutralize the surface charge. In the actual adsorption experiments, the initial Sr^{2+}-rich solution does not contain any ammonium ions; therefore, the exchange between Sr^{2+} ions and intercalated NH_4^+ ions should readily proceed.

These four samples were also analyzed by EDS to examine the composition of the predominant elements involved in the sorption experiments (Table S5). The continuous decrease in N due to additional washing with DIW supports the XRD results. A comparison of the amount of Sr and the change in N before and after the adsorption experiments reveals that the charge is balanced. This is because the charge ratio of the increase by Sr^{2+} adsorption to the decrease by NH_4^+ desorption is 1.008, which is close to unity. Two ammonium ions coordinated to the adsorbent surface could be released upon adsorption of Sr^{2+} to maintain electrical neutrality. According to the adsorption model proposed by Yamaguchi et al. [40], the as-prepared A-ZrP in the present study contains an excess amount of NH_4^+ compared to the apparent number of adsorption sites. The excess NH_4^+ is possibly released and exchanged with Sr^{2+}; a portion of the NH_4^+ ions covalently bonded to the phosphate preserves the crystalline structure. Therefore, ion exchange can be presumed to be the predominant mechanism for Sr^{2+} adsorption on A-ZrP.

The intercalated ammonium ions play a role in the enhancement of kinetics and the supply of active adsorption sites. The effect of a large interlayer spacing due to ammonium ions is evident, as described earlier. This kinetic enhancement drives the entire process of adsorption, which is mainly reaction-dependent. According to Yamaguchi et al. [40], nitrogen in ammonia favorably bonds to the hydrogen of the hydroxyl group that is covalently bonded to a phosphate group. The N/Zr molar ratio of the as-prepared A-ZrP reaches approximately 5.0 (Table S5). Because one covalently bonded ammonium ion corresponds to one Zr atom in A-ZrP ($Zr(NH_4PO_4)(HPO_4)\cdot 0.3H_2O$), a considerable amount of NH_4^+ should also coordinate with bridging oxygen atoms by hydrogen bonding. These excess ammonium sites first act as active sorption sites for Sr^{2+} ions because hydrogen bonding is appreciably

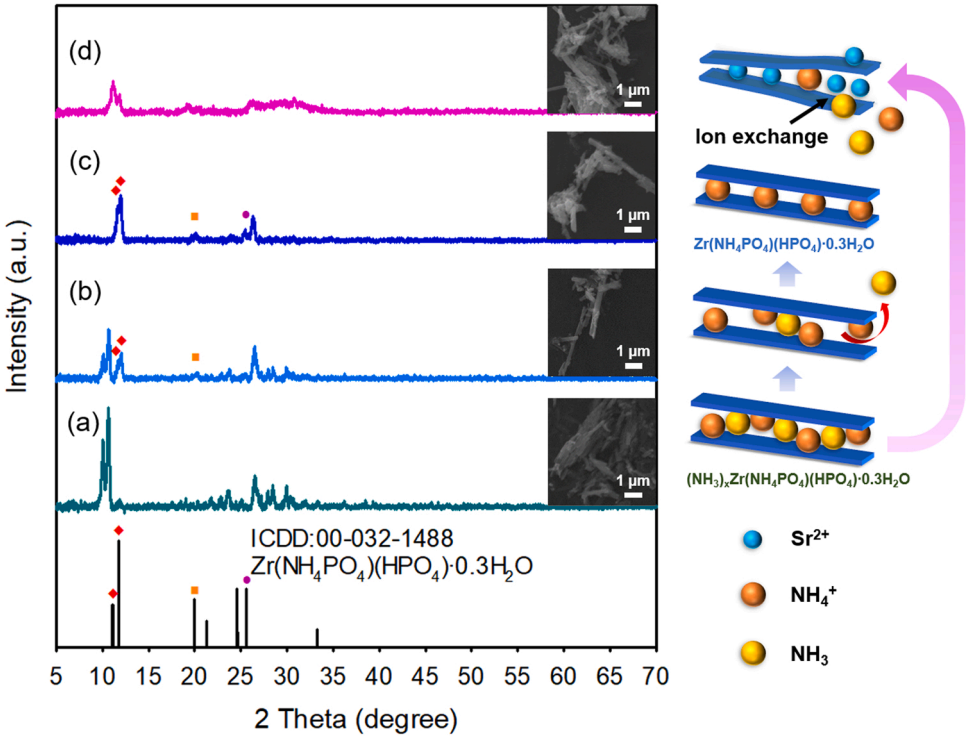

Fig. 5. XRD patterns, SEM images, and proposed mechanism for (a) as-prepared A-ZrP, A-ZrPs washed with DIW for (b) 1 h and (c) 4 h, and (d) Sr^{2+}-loaded A-ZrP.

weaker than covalent bonding, and the bridging oxygen atoms have more negative charge than the terminal oxygen [41]. The reaction based on these observations can be expressed by Eq. (12).

$$\equiv PO_4\cdots 2NH_4^+ + Sr^{2+} \leftrightarrow \equiv PO_4\cdots Sr^{2+} + 2NH_4^+ \quad (12)$$

Finally, the enhancement in Sr^{2+} adsorption onto A-ZrP was hypothesized to proceed via two interactions: electrostatic interactions and chemical affinity. Divalent Sr^{2+} ions have a slightly smaller ionic radius (1.18–1.44 Å) than NH_4^+ ions (1.40–1.67 Å), and consequently, the Coulombic interactions of Sr^{2+} with oxygen on the adsorbent surface amount to more than twice that of ammonium. Suh et al. [42] explained this adsorption behavior using the concept of chemical affinity or chemical hardness (η) [43]. The weakly-hard bridging O of A-ZrP prefers weakly hard Sr^{2+} (η = 16.3 eV) to NH_4^+, with NH_4^+ possibly having a slightly lower hardness than K^+ (η = 13.64 eV), based on the hardness of NH_3 (η = 8.2 eV) and the slightly larger size of NH_4^+ (1.40–1.67 Å) than that of K^+ (1.37–1.64 Å). Although O is generally regarded as a hard base element (η = 6.08 eV), the increased electron density on the bridging O [41] contributed to it being less hard [44]. These theories also account for the effect of coexisting ions on Sr adsorption. Although the η of Na^+ (21.08 eV) and K^+ ions are close to that of Sr^{2+}, their monovalent charge makes them less likely to be associated with the bridging O of A-ZrP. Among the divalent species investigated in this study, Mg^{2+} has a considerably higher hardness (η = 32.55 eV) than Sr^{2+}, resulting in restrictive interference with Sr^{2+} adsorption. At a Sr^{2+} dose of 10 mg L^{-1} (or 0.114 mmol L^{-1}), the Sr^{2+} adsorption decreases to 99.4% and 77.8% at 1 and 10 mmol L^{-1} of Mg^+, respectively (Fig. 4(d)). Conversely, Ca^{2+} with a hardness (η = 19.52 eV) similar to that of Sr^{2+} exhibits a more pronounced interference. At a Sr^{2+} dose of 10 mg L^{-1}, the Sr adsorption decreases to 95.5% and 37.4% at 1 and 10 mmol L^{-1} of Ca^{2+}, respectively. Although the concentrations of Ca^{2+} are ~9 and ~90 times that of Sr^{2+}, Sr^{2+} exhibits a significantly higher chemical affinity than Ca^{2+} for adsorption onto A-ZrP. These results demonstrate the remarkable association between Sr^{2+} ions and the phosphate of A-ZrP in terms of the chemical affinity or hardness among the various cations investigated in this study.

5. Conclusions

A whisker-like crystalline layered A-ZrP was successfully synthesized using a one-pot hydrothermal method and applied as a strontium adsorbent for the first time. A-ZrP exhibited a higher maximum adsorption capacity and faster adsorption kinetics than those of Na^+-intercalated ZrP owing to the intercalated ammonium ions possessing appropriate physicochemical characteristics for ion exchange with Sr^{2+}. In terms of kinetics, the intercalated NH_4^+ ions expanded the interlayer spacing of the layered adsorbent, thereby reducing the diffusion barrier of the adsorption sites. Moreover, the occupation of the active sites in advance by the NH_4^+ ions facilitated the subsequent adsorbate behavior. The electric charge and chemical hardness of NH_4^+ were well suited to act as advance guards. Therefore, the phosphate of A-ZrP preferred Sr^{2+} to NH_4^+. This explanation was also applicable to the negligible effect of coexisting cations on Sr^{2+} adsorption. Consequently, the maximum adsorption capacity (q_m = 341 mg g^{-1}) and selectivity ($K_d = 5.3 \times 10^5$ mL g^{-1} at a pH of 7) for Sr^{2+} were higher than those of several previously reported adsorbents. These results support the potential use of A-ZrP as an effective adsorbent in various environmental applications, such as the remediation of radioactive wastewater.

Funding

This work was supported by the National Research Foundation (NRF) grant funded by the Ministry of Science and ICT, Republic of Korea [grant number 2019R1A2C1084995]; the Basic Science Research Program through the NRF funded by the Ministry of Education, Republic of Korea [grant number 2020R1A6A1A03044834]; and the Basic Research Project of the Korea Institute of Geoscience and Mineral Resources (KIGAM) funded by the Ministry of Science and ICT of Korea.

CRediT authorship contribution statement

Zeqiu Li: Methodology, Formal analysis, Writing – original draft. **Eleazer L. Vivas:** Writing – review & editing. **Yong Jae Suh:** Validation, Investigation, Writing – review & editing. **Kuk Cho:** Conceptualization, Supervision, Funding acquisition.

Declaration of Competing Interest

The authors declare that they have no known competing financial interests or personal relationships that could have appeared to influence the work reported in this paper.

Appendix A. Supporting information

Supplementary data associated with this article can be found in the online version at doi:10.1016/j.jece.2022.107333.

References

[1] X. Zhang, Y. Liu, Nanomaterials for radioactive wastewater decontamination, Environ. Sci. Nano 7 (2020) 1008–1040, https://doi.org/10.1039/c9en01341e.
[2] R. Periáñez, K.-S. Suh, M. Byung-Il, N. Casacuberta, P. Masqué, Numerical modeling of the releases of 90Sr from Fukushima to the ocean: an evaluation of the source term, Environ. Sci. Technol. 47 (2013) 12305–12313, https://doi.org/10.1021/es4031408.
[3] S.K. Sahoo, N. Kavasi, A. Sorimachi, H. Arae, S. Tokonami, J.W. Mietelski, E. Lokas, S. Yoshida, Strontium-90 activity concentration in soil samples from the exclusion zone of the Fukushima daiichi nuclear power plant, Sci. Rep. 6 (2016) 23925, https://doi.org/10.1038/srep23925.
[4] H. Zhang, X. Zhou, L. Wang, W. Wang, J. Xu, Concentrations and potential health risks of strontium in drinking water from Xi'an, Northwest China, Ecotoxicol. Environ. Saf. 164 (2018) 181–188, https://doi.org/10.1016/j.ecoenv.2018.08.017.
[5] H. Peng, F. Yao, S. Xiong, Z. Wu, G. Niu, T. Lu, Strontium in public drinking water and associated public health risks in Chinese cities, Environ. Sci. Pollut. Res. 28 (2021) 23048–23059, https://doi.org/10.1007/s11356-021-12378-y.
[6] J. Zhao, L. Csetenyi, G.M. Gadd, Fungal-induced $CaCO_3$ and $SrCO_3$ precipitation: a potential strategy for bioprotection of concrete, Sci. Total Environ. (2021), 151501, https://doi.org/10.1016/j.scitotenv.2021.151501.
[7] S.M. Al-Jubouri, N.A. Curry, S.M. Holmes, Hierarchical porous structured zeolite composite for removal of ionic contaminants from waste streams and effective encapsulation of hazardous waste, J. Hazard. Mater. 320 (2016) 241–251, https://doi.org/10.1016/j.jhazmat.2016.08.011.
[8] L. Roshanfekr Rad, M. Anbia, Zeolite-based composites for the adsorption of toxic matters from water: a review, J. Environ. Chem. Eng. 9 (2021), 106088, https://doi.org/10.1016/j.jece.2021.106088.
[9] P. Trivedi, L. Axe, A comparison of strontium sorption to hydrous aluminum, iron, and manganses oxides, J. Colloid Interface Sci. 218 (1999) 554–563, https://doi.org/10.1006/jcis.1999.6465.
[10] L. Axe, T. Tyson, P. Trivedi, T. Morrison, Local structure analysis of strontium sorption to hydrous manganese oxide, J. Colloid Interface Sci. 224 (2000) 408–416, https://doi.org/10.1006/jcis.2000.6737.
[11] Z. Zhang, P. Gu, M. Zhang, S. Yan, L. Dong, G. Zhang, Synthesis of a robust layered metal sulfide for rapid and effective removal of Sr^{2+} from aqueous solutions, Chem. Eng. J. 372 (2019) 1205–1215, https://doi.org/10.1016/j.cej.2019.04.193.
[12] M. Zhang, P. Gu, Z. Zhang, J. Liu, L. Dong, G. Zhang, Effective, rapid and selective adsorption of radioactive Sr^{2+} from aqueous solution by a novel metal sulfide adsorbent, Chem. Eng. J. 351 (2018) 668–677, https://doi.org/10.1016/j.cej.2018.06.069.
[13] P. Amesh, A.S. Suneesh, K.A. Venkatesan, R. Uma Maheswari, S. Vijayalakshmi, Preparation and ion exchange studies of cesium and strontium on sodium iron titanate, Sep. Purif. Technol. 238 (2020), https://doi.org/10.1016/j.seppur.2019.116393.
[14] J. Ryu, S. Kim, H.-J. Hong, J. Hong, M. Kim, T. Ryu, I.-S. Park, K.-S. Chung, J. S. Jang, B.-G. Kim, Strontium ion (Sr^{2+}) separation from seawater by hydrothermally structured titanate nanotubes: removal vs. recovery, Chem. Eng. J. 304 (2016) 503–510, https://doi.org/10.1016/j.cej.2016.06.131.
[15] Y. Cheng, X. Dong Wang, S. Jaenicke, G.-K. Chuah, Mechanochemistry-based synthesis of highly crystalline γ-zirconium phosphate for selective ion exchange, Inorg. Chem. 57 (2018) 4370–4378, https://doi.org/10.1021/acs.inorgchem.7b03202.
[16] Y. Cheng, S.S. Chui, X.D.T. Wang, S. Jaenicke, G.K. Chuah, One-pot synthesis of layered disodium zirconium phosphate: crystal structure and application in the

remediation of heavy-metal-contaminated wastewater, Inorg. Chem. 58 (2019) 13020–13029, https://doi.org/10.1021/acs.inorgchem.9b01938.
[17] W. Mu, Q. Yu, R. Zhang, X. Li, R. Hu, Y. He, H. Wei, Y. Jian, Y. Yang, Controlled fabrication of flower-like α-zirconium phosphate for the efficient removal of radioactive strontium from acidic nuclear wastewater, J. Mater. Chem. A 5 (2017) 24388–24395, https://doi.org/10.1039/c7ta07803j.
[18] W. Mu, Q. Yu, J. Gu, X. Li, Y. Yang, H. Wei, S. Peng, Bonding of crown ethers to α-zirconium phosphate—novel layered adsorbent for radioactive strontium separation, Sep. Purif. Technol. 240 (2020), 116658, https://doi.org/10.1016/j.seppur.2020.116658.
[19] E. Kobayashi, A study of inorganic ion exchangers. VII. The synthesis of γ-$NH_4ZrH(PO_4)_2$ and ion-exchange properities of γ-$Zr(HPO_4)_2$•$2H_2O$, Bull. Chem. Soc. Jpn. 56 (1983) 3756–3760, https://doi.org/10.1246/bcsj.56.3756.
[20] V. Sidey, On the effective ionic radii for ammonium, Acta Crystallogr. Sect. B 72 (2016) 626–633, https://doi.org/10.1107/S2052520616008064.
[21] R. Shannon, Revised effective ionic radii and systematic studies of interatomic distances in halides and chalcogenides, Acta Crystallogr. Sect. A 32 (1976) 751–767, https://doi.org/10.1107/S0567739476001551.
[22] A. Anto Jeffery, C. Nethravathi, M. Rajamathi, Two-dimensional nanosheets and layered hybrids of MoS_2 and WS_2 through exfoliation of ammoniated MS_2 (M = Mo,W), J. Phys. Chem. C 118 (2014) 1386–1396, https://doi.org/10.1021/jp410918c.
[23] M. Yamaguchi, H. Miyaoka, Y. Kojima, Concentration–composition-isotherm for the ammonia absorption process of zirconium phosphate, RSC Adv. 10 (2020) 20882–20885, https://doi.org/10.1039/d0ra03817b.
[24] R.G. Pearson, Absolute electronegativity and hardness: application to inorganic chemistry, Inorg. Chem. 27 (1988) 734–740, https://doi.org/10.1021/ic00277a030.
[25] R.G. Pearson, Hard and soft acids and bases, J. Am. Chem. Soc. 85 (1963) 3533–3539, https://doi.org/10.1021/ja00905a001.
[26] Y. Cheng, X.T. Wang, S. Jaenicke, G.-K. Chuah, Minimalistic liquid-assisted route to highly crystalline α-zirconium phosphate, ChemSusChem 10 (2017) 3235–3242, https://doi.org/10.1002/cssc.201700885.
[27] J. Lin, L. Wang, Comparison between linear and non-linear forms of pseudo-first-order and pseudo-second-order adsorption kinetic models for the removal of methylene blue by activated carbon, Front. Environ. Sci. Eng. China 3 (2009) 320–324, https://doi.org/10.1007/s11783-009-0030-7.
[28] K.A. Syed, S.F. Pang, Y. Zhang, G. Zeng, Y.H. Zhang, Micro-Raman observation on the HPO_4^{2-} association structures in an individual dipotassium hydrogen phosphate (K_2HPO_4) droplet, J. Phys. Chem. A 116 (2012) 1558–1564, https://doi.org/10.1021/jp2110743.
[29] A.S. Khan, H. Khalid, Z. Sarfraz, M. Khan, J. Iqbal, N. Muhammad, M.A. Fareed, I. U. Rehman, Vibrational spectroscopy of selective dental restorative materials, Appl. Spectrosc. Rev. 52 (2016) 507–540, https://doi.org/10.1080/05704928.2016.1244069.
[30] V. Muñoz-Iglesias, M. Fernández-Sampedro, C. Gil-Lozano, L.J. Bonales, O. Ercilla Herrero, M.P. Valles González, E. Mateo-Martí, O. Prieto-Ballesteros, Characterization of NH_4-montmorillonite under conditions relevant to Ceres, Appl. Clay Sci. 209 (2021), 106137, https://doi.org/10.1016/j.clay.2021.106137.
[31] A. Dyer, D. Leigh, F.T. Ocon, Studies on crystalline zirconium phosphate-I: ion-exchanged forms of α-zirconium phosphate, J. Inorg. Nucl. Chem. 33 (1971) 3141–3151.
[32] A. Bashir, L.A. Malik, G.N. Dar, A.H. Pandith, Microwave-assisted hydrothermal synthesis of agglomerated spherical zirconium phosphate for removal of Cs^+ and Sr^{2+} ions from aqueous system, in: Inamuddin, M. Ahamed, A. Asiri (Eds.) Applications of Ion Exchange Materials in the Environment, 2019, pp. 95-108. https://doi.org/10.1007/978-3-030-10430-6_5.
[33] H.-J. Hong, J. Ryu, I.-S. Park, T. Ryu, K.-S. Chung, B.-G. Kim, Investigation of the strontium (Sr(II)) adsorption of an alginate microsphere as a low-cost adsorbent for removal and recovery from seawater, J. Environ. Manage. 165 (2016) 263–270, https://doi.org/10.1016/j.jenvman.2015.09.040.
[34] H. Chen, D. Shao, J. Li, X. Wang, The uptake of radionuclides from aqueous solution by poly(amidoxime) modified reduced graphene oxide, Chem. Eng. J. 254 (2014) 623–634, https://doi.org/10.1016/j.cej.2014.05.091.
[35] H.J. Hong, H.S. Jeong, B.G. Kim, J. Hong, I.S. Park, T. Ryu, K.S. Chung, H. Kim, J. Ryu, Highly stable and magnetically separable alginate/Fe_3O_4 composite for the removal of strontium (Sr) from seawater, Chemosphere 165 (2016) 231–238, https://doi.org/10.1016/j.chemosphere.2016.09.034.
[36] W. Mu, S. Du, Q. Yu, X. Li, H. Wei, Y. Yang, S. Peng, Highly efficient removal of radioactive ^{90}Sr based on sulfonic acid-functionalized α-zirconium phosphate nanosheets, Chem. Eng. J. 361 (2019) 538–546, https://doi.org/10.1016/j.cej.2018.12.110.
[37] J. Shin, Y.-G. Lee, J. Kwak, S. Kim, S.-H. Lee, Y. Park, S.-D. Lee, K. Chon, Adsorption of radioactive strontium by pristine and magnetic biochars derived from spent coffee grounds, J. Environ. Chem. Eng. 9 (2021), 105119, https://doi.org/10.1016/j.jece.2021.105119.
[38] J. Li, J. Jin, T. Zhang, W. Ma, X. Zeng, H. Sun, M. Cheng, M. Feng, X. Huang, Rapid and selective uptake of Cs^+ and Sr^{2+} ions by a layered thiostannate with acid–base and irradiation resistances, ACS ES&T Water 1 (2021) 2440–2449, https://doi.org/10.1021/acsestwater.1c00290.
[39] T. Wen, X. Wu, M. Liu, Z. Xing, X. Wang, A.W. Xu, Efficient capture of strontium from aqueous solutions using graphene oxide-hydroxyapatite nanocomposites, Dalton Trans. 43 (2014) 7464–7472, https://doi.org/10.1039/c3dt53591f.
[40] M. Yamaguchi, H. Miyaoka, Y. Kojima, Thermodynamic and spectroscopic analyses of zirconium phosphate-absorbed ammonia, J. Phys. Chem. C 125 (2021) 3758–3763, https://doi.org/10.1021/acs.jpcc.0c10882.
[41] L. Wang, W.H. Xu, R. Yang, T. Zhou, D. Hou, X. Zheng, J.H. Liu, X.J. Huang, Electrochemical and density functional theory investigation on high selectivity and sensitivity of exfoliated nano-zirconium phosphate toward lead(II), Anal. Chem. 85 (2013) 3984–3990, https://doi.org/10.1021/ac3037014.
[42] Y.J. Suh, J.W. Chae, H.D. Jang, K. Cho, Role of chemical hardness in the adsorption of hexavalent chromium species onto metal oxide nanoparticles, Chem. Eng. J. 273 (2015) 401–405, https://doi.org/10.1016/j.cej.2015.03.095.
[43] R.G. Parr, R.G. Pearson, Absolute hardness: companion parameter to absolute electronegativity, J. Am. Chem. Soc. 105 (1983) 7512–7516, https://doi.org/10.1021/ja00364a005.
[44] R.G. Pearson, Chemical hardness and density functional theory, J. Chem. Sci. 117 (2005) 369–377, https://doi.org/10.1007/BF02708340.